www.small-structures.com

Addressing Fundamental Challenges of Si/Gr Electrodes with High Silicon Contents Using Innovative Bilayer Electrode Structure Design

Jeong Hyeon Yoo, Sung Joon Park, Cheol Bak, Yong Min Lee,* and Ki Jae Kim*

The extremely high volume change of Si during alloying and dealloying in the charge/discharge process is a key challenge for increasing the Si content in Si/Gr electrodes. To address these fundamental challenges, a sophisticated bilayer Si/Gr electrode composed of an upper layer with a porous structure and a lower layer with a compact structure to increase the Si content while enhancing the long-term cycling stability of the electrode is designed. The unique structure of the bilayer Si/Gr electrode is achieved by controlling the densities of the upper and lower electrode layers. The porous structure of the upper layer can accommodate the volume expansion of Si, thereby increasing the Si content of the Si/Gr electrode. The compact structure of the lower layer can suppress the delamination of the electrode by the volume expansion of Si due to its high binding strength with the current collector, thus ensuring the long-term stability of the Si/Gr electrode. Consequently, because of the distinct features of the upper and lower layers in the bilayer Si/Gr electrode, superior cyclability is achieved despite an increase in the total Si content to 30 wt% in the Si/Gr electrode, with a specific capacity of 534.8 mAh g⁻¹ after 100 cycles.

J. H. Yoo, S. J. Park, K. J. Kim Department of Energy Science Sungkyunkwan University

Suwon, Gyeonggi-do 16419, Republic of Korea

E-mail: kijaekim@skku.edu

C. Bak, Y. M. Lee

Department of Energy Science & Engineering

Daegu Gyeongbuk Institute of Science and Technology (DGIST)

Daegu 42988, South Korea

E-mail: yongmin@yonsei.ac.kr

Y. M. Lee

Department of Chemical and Biomolecular Engineering

Yonsei University

Seoul 03722, Republic of Korea

K. J. Kim

SKKU Institute of Energy Science and Technology (SIEST)

Sungkyunkwan University

Suwon 16419, Republic of Korea

The ORCID identification number(s) for the author(s) of this article can be found under https://doi.org/10.1002/sstr.202400433.

© 2024 The Author(s). Small Structures published by Wiley-VCH GmbH. This is an open access article under the terms of the Creative Commons Attribution License, which permits use, distribution and reproduction in any medium, provided the original work is properly cited.

DOI: 10.1002/sstr.202400433

1. Introduction

Although lithium-ion batteries (LIBs) have attracted notable attention owing to their long-term cycling performance and low self-discharge, their energy density must be increased to meet the demands of electric vehicle and energy storage system applications.[1-14] To increase the energy density of LIBs, the graphite-based negative electrode should be replaced with a silicon (Si)-based anode because Si possesses a high specific capacity (3579 mAh g⁻¹) and low redox potential (0.4 V versus Li/Li⁺) and is abundantly available in nature. Despite these advantages, the practical utilization of Si as an anode material is challenging because the structural instability of the electrode originating from the severe volume expansion (up to 300%) of Si during the lithiation/delithiation process accelerates electrode deterioration, which

notably shortens the cycle life of the Si electrode. [15–20] Many efforts, such as the structural engineering of Si, alloying with foreign metal atoms, utilizing carbon materials, and developing polymeric binders, have been made to alleviate the volume change of Si during the charge/discharge steps. [21–28] Despite these efforts to mitigate the volume expansion of pure Si electrodes, the use of pure Si electrodes is still challenging because the aforementioned strategies cannot perfectly suppress the volume expansion of pure Si and require additional processes with high costs (e.g., making structures on Si particles, manufacturing functionalized binders, or alloying with other atoms), which are difficult for practical applications. [29–32]

An attractive strategy to overcome this drawback of pure Si electrodes is the addition of a small amount of Si to commercial graphite electrodes (denoted as Si/Gr electrodes) because of the synergetic effect of Si with a high theoretical capacity and graphite with electrical conductivity and structural stability. [33–42] Such Si/Gr electrodes have higher specific capacities than pure graphite electrodes; therefore, Si/Gr electrodes with a certain amount of Si have been used in conventional LIBs. However, when introducing a large amount of Si into a graphite electrode, the huge volume expansion of Si in the pure Si electrode leads to complication; therefore, a low quantity of Si (less than 10 wt%) is currently used in conventional LIBs. [43–45] Recently, several Si/Gr electrodes have been designed to increase the Si content in the Si/Gr electrode and ensure cycling stability. For example,

structu<u>re</u>

www.advancedsciencenews.com www.small-structures.com

Guo et al. used functionally graded materials to alleviate delamination between the anode materials and the current collector and to reduce the charge transport barrier. [46] Furthermore, Zhang et al. proposed a parabolic-gradient Si/Gr electrode, where the Si particles were condensed in the middle layer, thus effectively distributing the stress applied to the electrode and preventing electrode cracking and exfoliation. [47] Based on a review of previous studies, to increase the Si content in the Si/Gr electrode and ensure the stability of the Si/Gr electrode, the following key factors should be considered when designing the Si/Gr electrode. 1) An adequate empty space commensurately proportional to the silicon is provided to not only accommodate the volume expansion but also enhance the efficiency of lithium ion transport. 2) A higher adhesive strength with the current collector and lower silicon content in contact with it helps reduce electrode delamination.

Inspired by these approaches, we designed a sophisticated bilayer Si/Gr electrode composed of an upper layer with a porous structure and a lower layer with a compact structure. A bilayer Si/Gr electrode was fabricated by controlling the compact density of the upper and lower layer electrodes. Because of the porosity gradient of the Si/Gr electrode, the upper layer with a porous

structure was designed to contain a large quantity of Si and the lower layer with a compact structure was designed to contain a less quantity of Si (Figure 1a). Specifically, the lower layer, which has a compact structure and a less quantity of Si, exhibits less volume expansion owing to its lower Si content, thus maintaining a high binding strength with the Cu current collector during repeated charge/discharge cycles. These characteristics of the lower layer can alleviate delamination of the Si/Gr electrode from the Cu current collector, which can ensure electrode stability even after long-term cycling. The upper layer with high porosity not only leads to the enhancement of Li-ion transportation but also acts as a buffer layer to accommodate large volume expansion, enabling the presence of a large amount of Si (Figure 1b). Owing to the synergistic effect of the upper and lower layers, the proposed bilayer Si/Gr electrode exhibited a capacity of 452.3 mAh g⁻¹ after 100 cycles, even at a high loading level of $7.1 \,\mathrm{mg}\,\mathrm{cm}^{-2}$. Even with an increase in the Si content to 30 wt% of the overall electrode, the asymmetrically designed bilayer electrode could be stably operated for 100 cycles with an areal capacity of 2.67 mAh cm⁻². The bilayer Si/Gr electrode composed of an upper layer and a lower layer with a PGE in this study is a promising design for increasing the Si content in a Si/Gr

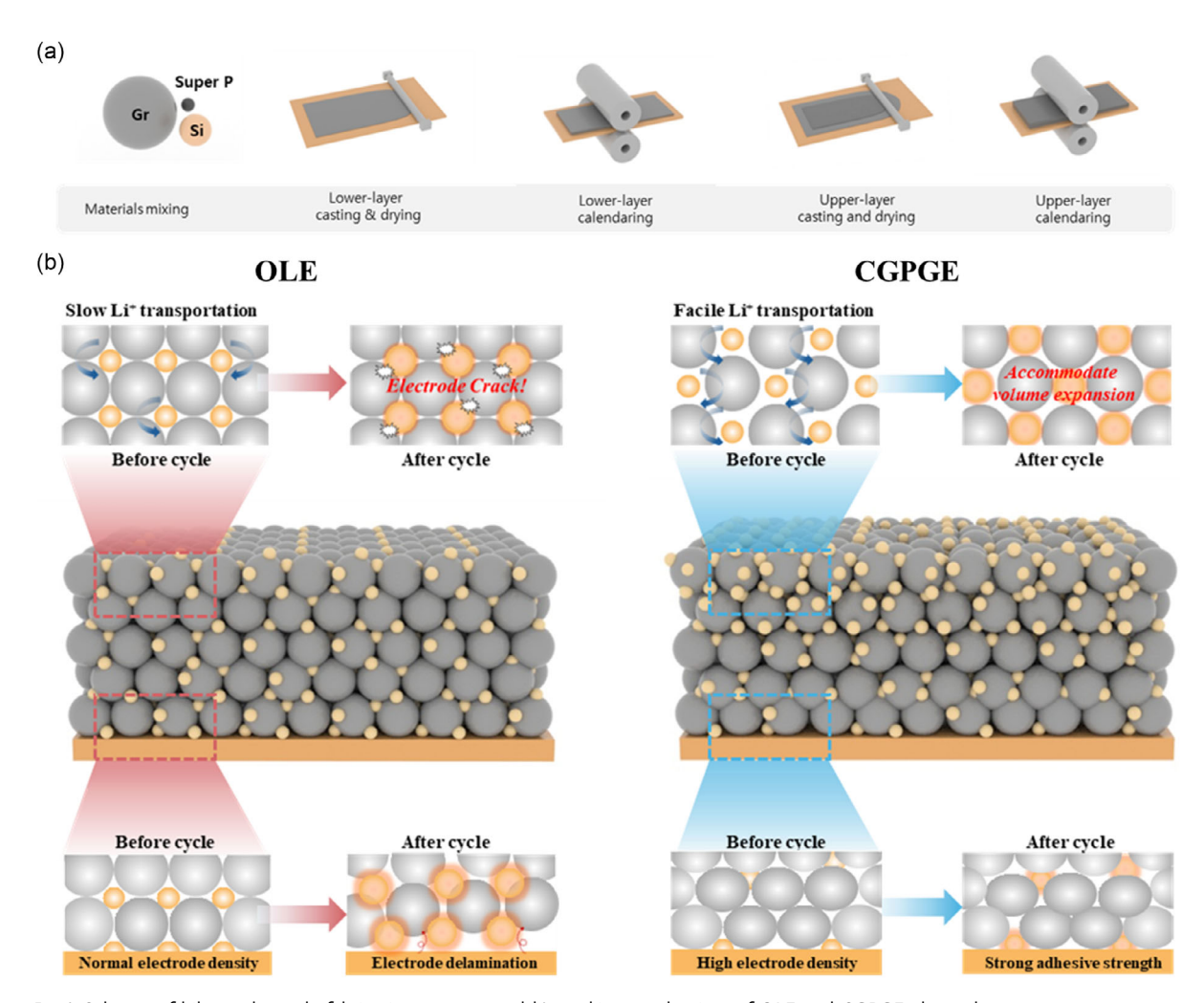


Figure 1. a) Scheme of bilayer electrode fabrication process and b) working mechanism of OLE and CGPGE electrode.

small structures

www.advancedsciencenews.com www.small-structures.com

electrode while also enhancing the long-term cycling stability of the Si/Gr electrode under industry-friendly conditions.

2. Results and Discussion

To demonstrate the superiority of the bilayer Si/Gr electrode with both porosity and Si content gradients (CGPGE), four Si/Gr electrodes with different structures were carefully prepared for comparison as follows: 1) Thus, the one-layer Si/Gr electrode is one layer electrode (OLE), 2) and bilayer Si/Gr electrode without both porosity and Si content gradients bilayer electrode (BLE), 3) bilayer Si/Gr electrode with only a porosity gradient (PGE), and 4) bilayer Si/Gr electrode with only Si component gradient (CGE). A schematic of the detailed structure and information on the five samples is shown in Figure S1 and Table S1, Supporting Information. To confirm the formation of the intentionally designed electrode structure, cross-sectional scanning electron microscopy (SEM) images of each electrode were obtained. As shown in Figure 2a–o, the electrode thickness of all samples was measured to be 65–66 µm with fixed overall

electrode density of 1.1 g cc⁻¹. In the energy-dispersive spectroscopy (EDS) images, Si and C are equally distributed in the OLE, BLE, and PGE because there is no component gradient in these electrodes. In contrast, the CGE and CGPGE showed higher Si contents in the upper layer and lower Si contents in the lower layer, where the Si component gradient was well made, as designed. Further, 3D X-ray microscopy (XRM) analysis was conducted to reveal the formation of the porosity gradient in PGE and CGPGE. Based on 3D visualization of the internal porosity of the electrode, the porosity gradient is shown in Figure 2p-y. The pores in OLE, BLE, and CGE are uniformly distributed without significant difference in the range of 10-60 µm from the current collector. Notably, the results showing evenly distributed pores in the BLE and CGE, which were fabricated by two pressing processes, indicated that the pore structure of the lower layer was not affected by the second pressing process, as intended. However, PGE and CGPGE have an electrode structure composed of an upper layer with high porosity and a lower layer with low porosity, suggesting that the different pore structures between the upper and lower layers were designed by a controlled pressing process. Consequently, based on the results of the

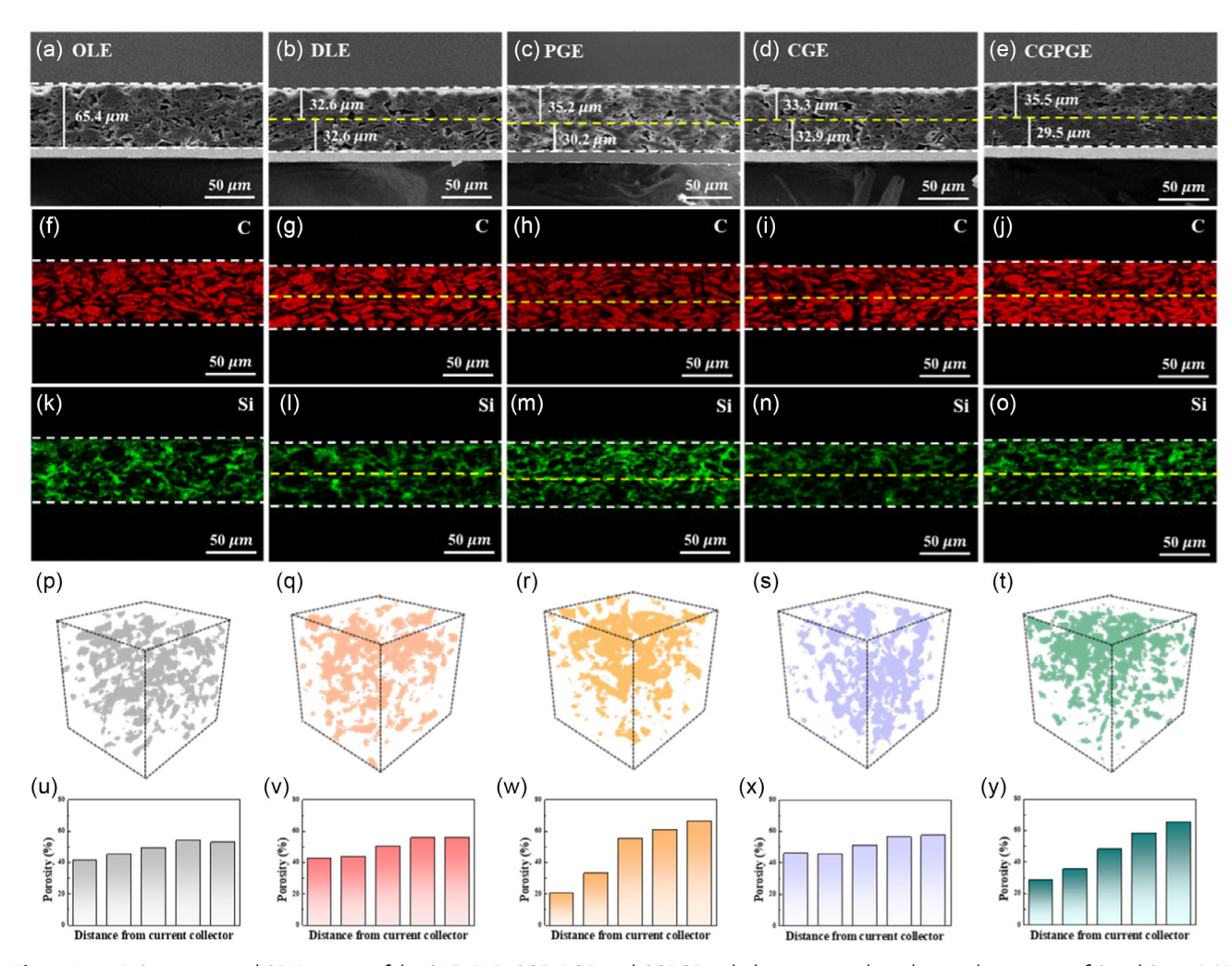


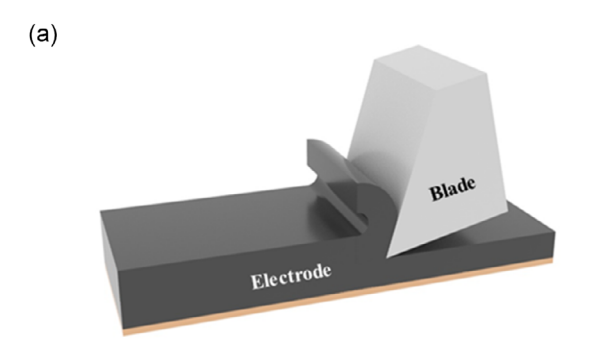
Figure 2. a—o) Cross-sectional SEM images of the OLE, BLE, CGE, PGE, and CGPGE with the corresponding elemental mappings of C and Si. p—t) 3D pore distribution in the electrode through XRM. u–y) porosity variation in the electrode according to distance from the current collector.

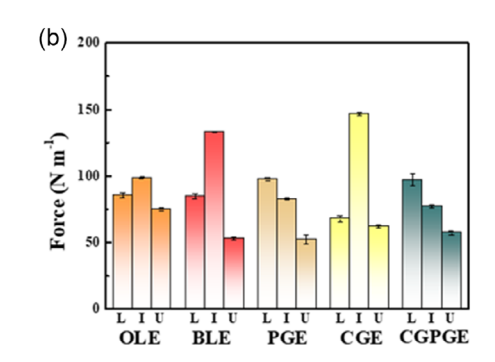
small structures

www.advancedsciencenews.com www.small-structures.com

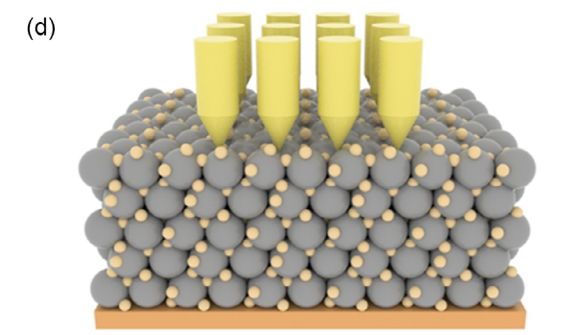
elemental distribution in the cross-sectional SEM images and XRM data analysis, the Si/Gr electrode with a Si content and porosity gradient was confirmed to be successfully designed through a controlled electrode manufacturing process.

Especially for bilayer electrodes, an inhomogeneous binder distribution might be formed at the interface between the upper and lower layers because the upper layer slurry penetrates the lower layer during the electrode manufacturing process. Thus, to investigate the binder distribution inside the electrode, which can be determined by the binding strength at a specific depth and location, we utilized a surface and interfacial characterization analysis system (SAICAS) (Figure 3a). [48] The SAICAS measurements were performed at three points of 10, 30, and 50 µm away from the current collector (Figure 3b.c). The measured values at 10 and 50 µm signified the binding strength of a lower layer and an upper layer and the measured value at 30 µm implied the binding strength of the interface between the lower layer and upper layer. The OLE showed a uniform binding strength in the upper layer, interface, and lower layer because of the even dispersion of the binder originating from the one-step electrode fabrication. However, for BLE and CGE, the binding strength at the interface between the upper and lower layers was higher than that for OLE. This is ascribed to the formation of a binder agglomerated layer at the interface layers of BLE and CGE because the solvent and binder of the electrode slurry seep into the lower layer with a porous structure during the drying step after casting the upper layer. Meanwhile, for PGE and CGPGE, the binding strength decreased linearly from the lower to the upper layer. This is because the upper layer has a weak binding strength owing to its relatively porous structure, whereas the lower layer has a strong binding strength owing to its relatively compact structure. The binding strength at the interface between the upper and lower layers of PGE and CGPGE did not increase compared to those of BLE and CGE. This result implies that a binder-agglomerated layer was not formed at the interface between the upper and lower layers of PGE and CGPGE, because the solvent and binder of the electrode slurry could not easily permeate into the lower layer owing to the compact structure of PGE and CGPGE during the drying step after upper layer casting. As the binder agglomeration layer





(c)								
			OLE	BLE	PGE	CGE	CGPGE	
	Distance from current collector		SAICAS force (N m ⁻¹)					
	Upper	(50 μm)	74.8	53.0	52.2	59.7	57.3	
	Interface	$(30~\mu\mathrm{m})$	98.6	132.9	82.7	121.3	77.3	
	Lower	$(10 \ \mu m)$	85.4	84.9	97.5	95.3	96.9	



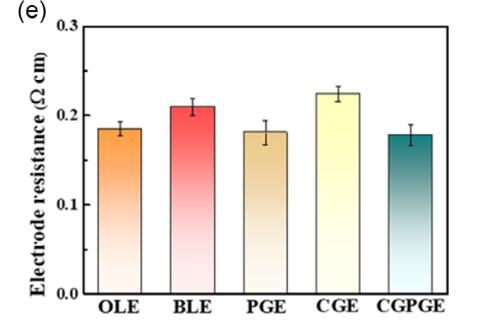


Figure 3. a) Measurement of binding strength for composite electrodes from SAICAS. b) Force on the vertical position in OLE, BLE, PGE, CGE, and CGPGE. c) SAICAS force on the vertical position in OLE, BLE, PGE, CGE, and CGPGE. d) Electrode resistance measurement equipment and e) corresponding resistance results of all samples.

26884062, 2025, 2, Downloaded from https://onlinelibrary.wiley.com/doi/10.1002/sstr.202400433 by Daegu Gyeongbuk Institute Of, Wiley Online Library on [18/02/2025]. See the Terms

conditions) on Wiley Online Library for rules of use; OA articles are governed by the applicable Creative Commons

inside the electrode is likely to increase the electrode resistance, we measured the electrode resistance using an electrode resistance measurement system under dry conditions (Figure 3d). $^{[49]}$ As shown in Figure 3e, the BLE (0.209 Ω cm) and CGE (0.224 Ω cm) exhibit increased resistance compared to the OLE (0.185 Ω cm), which can be explained by the binder-agglomerated region formed during the upper layer manufacturing process. Conversely, the measured resistance values of PGE (0.181 Ω cm) and CGPGE (0.178 Ω cm) were similar to that of OLE (0.185 Ω cm) because of the absence of the binder agglomeration layer inside the electrodes.

The effect of the component and porosity gradient between the upper and lower layer on electrochemical performance was revealed by cycling performance of Li||Si/Gr half-cell test at 0.2 C rate in a voltage range from 0.005 to 1.5 V with a high mass loading level of 7.1 mg cm $^{-2}$ (1.0 C = 694.8 mA g $^{-1}$). As presented in **Figure 4**a, the CGPGE delivered the highest discharge capacity of 666.0 mAh g $^{-1}$ at the first cycle (OLE: 620.1, BLE: 611.8, PGE: 653.1, CGE: 662.0 mAh g $^{-1}$). The increased initial capacity of CGPGE can be reasonably explained by the electrode structure. The mobility of lithium migration within an electrode increases with the porosity, and an electrode with a PGE can

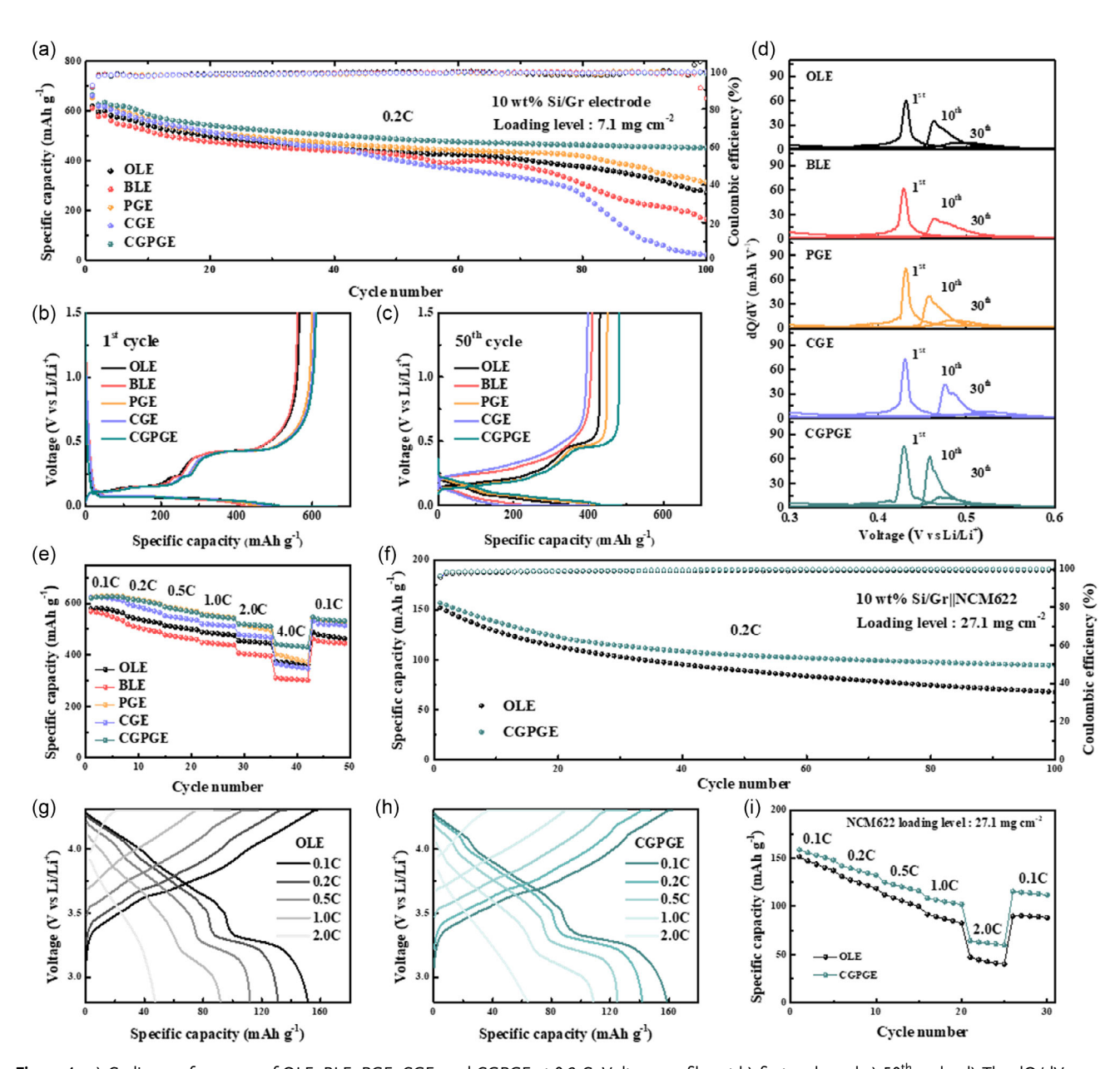


Figure 4. a) Cycling performance of OLE, BLE, PGE, CGE, and CGPGE at 0.2 C. Voltage profiles at b) first cycle and c) 50th cycle. d) The dQ/dV curves of OLE, BLE, CGE, PGE, and CGPGE at 1st, 10th, and 30th cycle. e) Rate performance from 0.1 to 4.0 C of prepared electrodes. f) Cycling performance of Si/Gr||NCM622 full cell with OLE and CGPGE at 0.2 C. Voltage profiles of Si/Gr||NCM622 full cell with g) OLE and h) CGPGE. i) Rate performance of Si/Gr||NCM622 full cell-equipped OLE and CGPGE from 0.1 to 2.0 C.

www.advancedsciencenews.com www.small-structures.com

engage in additional reactions with lithium. [40] Furthermore, as the fast surface reaction of Si increases the mobility of Li ions in the Si/Gr electrode, the higher Si content in the upper layer leads to improved Li transport into the electrode. [50] Benefiting from the harmonious effects of porosity and component gradient, CGPGE exhibited the highest reactivity, as shown in Figure S2, Supporting Information. Furthermore, in the repeated charge/ discharge process, CGPGE exhibited the lowest overpotential, as shown in the voltage profiles of all samples (Figure 4b.c). This is mainly attributed to the relatively lower electrolyte and charge transfer resistances of the CGPGE compared to those of the other electrodes (Figure S3, Supporting Information). Even after 100 cycles, the CGPGE delivered a high discharge capacity of 452.3 mAh g⁻¹ because of its electrode stability, whereas the other electrodes underwent severe capacity loss (OLE: 272.8, BLE: 167.3, PGE: 315.9, and CGE: 22.9 mAh g⁻¹). The increased electrode stability was further confirmed by the dQ/dV plot, which contained information about electrode degradation through the peak intensity and location. As the reaction voltage range of graphite and Si overlaps, where it cannot be distinguished for each reaction individually, we analyzed the delithiation process to determine the reaction of Si only, which is the major component leading the Si/Gr electrode to the failure mode (Figure S4, Supporting Information).^[51,52] In all samples except CGPGE, a severe decrease in the peak intensity and location shift occurred because of the increased internal resistance caused by electrode deterioration (Figure 4d). The lowest degradation of CGPGE was further supported by the electrochemical impedance spectroscopy (EIS) results after 50 cycles, in which CGPGE showed the lowest resistance (Figure S5. Supporting Information). Additionally, the Warburg impedance data indicate that CGPGE exhibits improved lithium-ion diffusivity, which can be attributed to its electrode architecture (Figure S6 and Table S2, Supporting Information, calculated using Equation S1 and S2, Supporting Information). As depicted in Figure 4e and Figure S7, Supporting Information, originating from the facile transportation of lithium ion, the CGPGE shows the highest capacity of 442.7 mAh g^{-1} at 4.0 C rate (OLE: 375.1 mAh g^{-1} , BLE: 311.6 mAh g^{-1} , PGE: 402.0 mAh g^{-1} , and CGE: 366.6 mAh g^{-1}).

To assess the effect of the electrode structure under practical conditions, a full cell incorporating a Si/Gr anode coupled with a LiNi_{0.6}Co_{0.2}Mn_{0.2}O₂ (NCM622) cathode at a loading level of 27.1 mg cm⁻² was assembled with an N/P ratio of 1.1 (1.0 C = 200 mA g⁻¹).^[53] Figure 4f displays the long-cycle performance of the full cell equipped with the OLE and CGPGE anodes and the NCM622 cathode. In the initial charge and discharge process at 0.1 C rate, the full cell with CGPGE delivered $171.2 \,\mathrm{mAh}\,\mathrm{g}^{-1}$ which was higher than that of OLE (168.6 mAh g⁻¹) with an enhanced initial Coulombic efficiency (CGPGE: 85.9% and OLE: 84.8%) as shown in Figure S8. Supporting Information. Furthermore, the full cell with CGPGE showed higher capacity retention after 100 cycles owing to enhanced Si/Gr anode stability (CGPGE: 94.15 mAh g⁻¹ and OLE: 67.70 mAh g⁻¹). The full cell with CGPGE shows significantly higher specific discharge capacity even at 2.0 C rate $(64.37 \text{ mAh g}^{-1})$ than that of OLE $(47.3 \text{ mAh g}^{-1})$ as shown in Figure 4g-i. This reveals that the distinctive bilayer structure was electrochemically effective for both half and full cells with a practical N/P ratio.

To confirm our hypothesis that the enhanced electrochemical performance of the CGPGE originates from the distinguished bilayer structure composed of an upper layer with a porous structure and a lower layer with a compact structure, all electrodes were probed by postmortem analysis of cross-sectional SEM images before and after 50 cycles. The poor cycle performance of Si/Gr electrodes originates from electrode delamination from the current collector and electrode isolation due to the huge expansion of Si during repeated charge/discharge cycles. As shown in Figure 5a-j, electrode delamination from the current collector and electrode cracking were observed in all samples, except for CGPGE. In the case of OLE, severe electrode delamination from the current collector and severe cracking of the electrode, which is a typical degradation behavior of conventional Si/Gr electrodes, clearly appeared after 50 cycles, leading to accelerated deterioration of the electrode and poor cycle performance. BLE and CGE were more severe than OLE and, they also exhibited electrode delamination from the current collector, accompanied by electrode cracking after 50 cycles. However, the PGE with enhanced binding strength with the current collector, originating from the high compact density of the lower layer, showed relieved electrode delamination. CGPGE maintained stable contact with the current collector owing to its strong binding strength with the current collector of the lower layer with low Si content, rendering it immune to detachment from the current collector.

In addition, surface cracking of the electrode was observed using SEM, as shown in Figure 5k-o. The surfaces of the OLE and BLE showed typical surface cracking of the conventional Si/Gr electrode owing to the large volume expansion of the Si particles during cycling. In the case of CGE, the increased Si content in the upper layer without sufficient space leads to severe surface cracking because the stress from the huge volume expansion of the upper layer cannot be relieved. However, surface cracking on the electrode was not observed for the PGE and CGPGE because the upper layer with high porosity can relax the huge volume expansion of the Si particles through repeated lithiation/delithiation. Through postmortem analysis, we visualized the role of the porosity and component gradients in maintaining electrode stability by cross-sectional and top-view SEM observations. Because of the combined unique features of porosity and component gradients, we assume that CGPGE has superior electrochemical performance without crucial electrode degradation during repeated charge/discharge processes compared to other electrodes.

Based on previous experimental results, the carefully designed CGPGE exhibited enhanced electrochemical performance and high stability. Thus, we synthesized electrodes with Si content of up to 30 wt% (1.0 C = 1340.4 mA g $^{-1}$). Even with the increased Si content of the Si/Gr electrode, CGPGE had the lowest charge/discharge overpotential according to the voltage profiles shown in **Figure 6**a,b. Furthermore, the CGPGE delivered a superior discharge capacity of 1329.8 mAh g $^{-1}$ compared to that of the OLE (1179.9 mAh g $^{-1}$) at first cycle. After 100 cycles, CGPGE still had a higher capacity of 534.8 mAh g $^{-1}$ than that of OLE (396.9 mAh g $^{-1}$), as shown in Figure 6c. These results confirm that they are due to the significant structural properties that

26884062, 2025, 2, Downloaded from https://onlinelibrary.wiley.com/doi/10.1002/sstr.202400433 by Daegu Gyeongbuk Institute Of, Wiley Online Library on [18/02/2025]. See the Terms

on Wiley Online Library for rules of use; OA articles are governed by the applicable Creative Commons

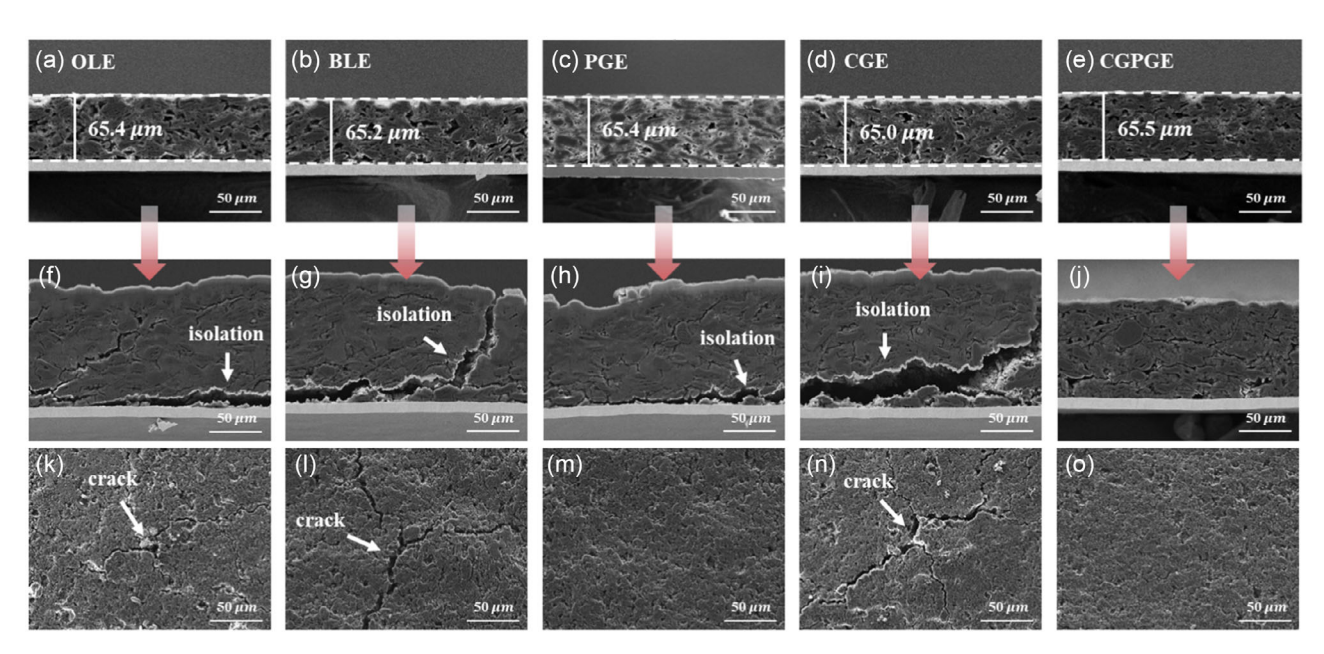


Figure 5. a-e) Cross-sectional SEM images of the OLE, BLE, PGE, CGE, and CGPGE before cycle. f-j) After 50 cycles. k-o) Top-view SEM images of the OLE, BLE, PGE, CGE, and CGPGE after 50 cycles.

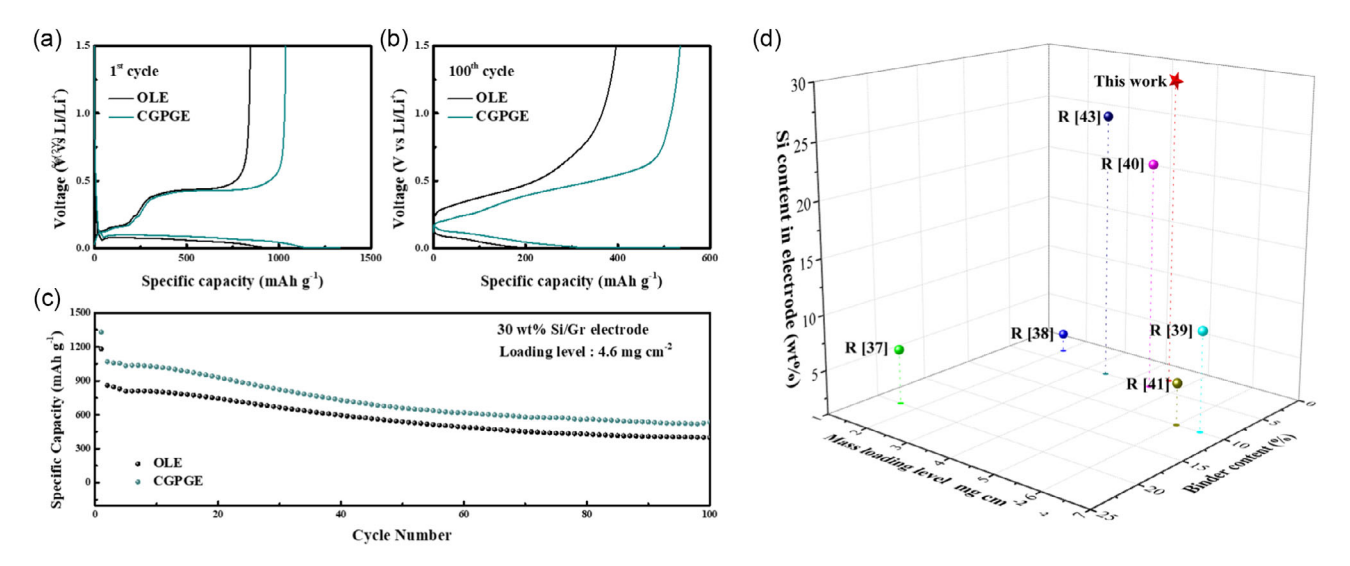


Figure 6. a) Charge/discharge voltage profiles of OLE and CGPGE at (a) 1st cycle and b) 50th cycle. c) Cycling performance of Si/Gr electrode with increased Si component to 30 wt% at 0.2 C. d) Comparison of material content and mass loading level reported in previous study.

reduce electrode deterioration: 1) the high binding strength between the lower layer and the current collector, along with a lower proportion of Si, alleviates delamination from the current collector owing to volume expansion and 2) the upper layer with high porosity increases the ability to accommodate volume change and Li diffusivity within the electrode because its high Si content enables more reactions. As shown in Figure 6d, our experiment was conducted with a relatively high silicon content, low binder content, and high mass loading level and it demonstrated excellent performance through previous analysis even under harsh circumstances. This further implies that the

suggested electrode structure design using porosity and component gradients enables the development of Si/Gr electrodes with high Si content under strict conditions.

3. Conclusion

In this study, we propose a sophisticated bilayer Si/Gr electrode with a threefold increase in Si content compared to the conventional Si/Gr electrode, with concurrent stable long-term cycling performance. The porous structure of the upper layer in the www.advancedsciencenews.com www.small-structures.com

small structures

CGPGE can act as a buffer to accommodate the large volume expansion of the Si particles, thus increasing the Si content. Therefore, despite the increased Si content, the typical electrode cracking that occurs on the surface of the Si/Gr electrode, which is one of the major causes of poor cycling performance of the Si/Gr electrode, is effectively suppressed in the CGPGE. Concurrently, the compact structure and lower Si content of the lower layer in the CGPGE can increase the binding strength between the Si/Gr electrode and the Cu current collector and alleviate electrode delamination due to the severe volume expansion of Si particles. Thus, the combined effects of the lower layer in the CGPGE can successfully prevent electrode delamination from the Cu current collector, which is another reason for the degradation in cycling performance. Due to the unique function of the upper layer and lower layer, the cell with CGPGE exhibited high discharge capacity of 452.3 mAh g⁻¹ after 100 cycles. In addition, CGPGE still showed superior cycling stability for 100 cycles, even under the harsh conditions of increased Si content to 30 wt%. Consequently, the porosity gradient design of the Si/Gr electrode, enabling the tailoring of the Si content according to the porosity, suggests an industry-friendly strategy toward a robust Si/Gr electrode design and holds promise as a platform technology for the development of high-energy-density LIBs.

4. Experimental Section

Materials: The starting materials used were silicon (Avention, 100 nm), graphite (BTR 918-2, D50 = 17.42), sodium carboxymethyl cellulose (CMC), styrene-butadiene rubber (SBR), and Super P.

Electrode Fabrication: The material ratio in all electrodes was the same: Si: Gr = 10:90 wt%; carbon black, CMC, and SBR in a weight ratio of 96:1:1:2. Additionally, the overall electrode density of all the electrodes was the same at 1.1 g cc $^{-1}$.

OLE was obtained by coating Cu current collector with a slurry (in a ratio of Si: Gr = 10:90) and drying for 3 h at 100 °C. The lower layer of layer electrode was cast on Cu current collector from a slurry (Si: Gr = 10:90) with half the OLE loading and dried for 3 h at 100 °C, further, and pressed to 1.1 g $\,\mathrm{cc^{-1}}$. The upper layer of the electrode was coated onto the dried lower layer with the same slurry ratio (Si: Gr = 10.90). The lower layer of CGE was cast on Cu current collector from a slurry (Si: Gr = 7.5:92.5) with half the OLE loading, dried for 3 h at 100 °C, and then pressed to 1.1 g cc^{-1} . The upper layer of the electrode was coated onto the dried lower layer with a slurry of different ratios (Si: Gr = 12.5:87.5) to obtain the CGE. The lower layer of PGE was cast on Cu current collector with half the OLE loading of the slurry (Si: Gr = 10:90), dried for 3 h at 100 °C, and then pressed at 1.2 g cc⁻¹ to have a PGE within entire electrode. The upper layer of the electrode was coated onto the dried lower layer with the same slurry ratio (Si: Gr=10.90). The lower layer of CGPGE was cast on Cu current collector as a slurry (Si: Gr = 7.5:92.5) with half the OLE loading, dried for 3 h at 100 °C, and then pressed to 1.2 g cc⁻¹ to have a PGE within entire electrode. The upper layer was coated onto the dried lower layer with a different slurry ratio (Si: Gr = 12.5:87.5), resulting in a CGE within the entire electrode. Finally, all samples were dried overnight at 100 °C, pressed to an overall electrode density of 1.1 g cc⁻¹, and electrode fabrication was completed.

The OLE with 30 wt% Si content within the electrode increased the Si content and the manufacturing process was the same as that for the OLE sample with 10 wt% Si content. For the CGPGE samples with a Si content of 30% within the electrode, the casting and pressing processes were the same as those for the CGPGE sample with 10 wt% Si content; however, the Si content of the lower electrode was 20 wt% and the Si content of the upper electrode was 40 wt%. Hence, a difference was observed in the Si ratio of each layer.

LiNi $_{0.6}$ Co $_{0.2}$ Mn $_{0.2}$ O $_{2}$ (NCM622) electrode fabrication: LiNi $_{0.6}$ Co $_{0.2}$ Mn $_{0.2}$ O $_{2}$ (NCM 622) electrode was prepared by slurry casting onto an Al current collector. The slurry consisted of NCM powder, Super P (Timcal), and a polyvinylidene fluoride (PVDF) binder (KF1100, MW = 280 000) in a mass ratio of 95:2:3 in an N-methyl-2-pyrrolidone solution (Junsei Chemical Japan). The resulting electrode sheet was dried at 100 °C for 12 h in a vacuum oven.

Characterization of the Structure and Properties: Field-emission scanning electrode microscope (JEOL Company JSM 7000 F) was used to observe changes in the morphology of the electrode samples. The cross-sectional images of the samples were obtained after polishing using an ion-beam cross-sectional polisher (CP, JEOL Company SM 09010). The elemental compositions of the sample surfaces and cross sections were measured using EDS. SAICS (SAICAS-DN; Daipla Wintes, Japan) was used to measure the binding strengths of the electrodes. The bulk binding strengths within electrodes were repeatedly measured at every 10 µm depth from the surface with a boron nitride blade (width: 1 mm, rake angle: 20°, and clearance angle: 10°). The blade moved in the horizontal and vertical directions at 2.0 and 0.2 µm s⁻¹, respectively. As described in the measurement procedure, the blade was first aligned parallel to the electrode surface. Without this alignment, the reliability of the measurement data was greatly reduced. Thereafter, the electrode was cut to reach the desired depth or interface and the horizontal force measured in the peeling mode was averaged and converted into a binding force. A Carl Zeiss Xradia 620 Versa 3D XRM was used for nondestructive imaging. XRM radiates X-rays to an observation sample and uses the intensity distribution of the transmitted X-rays passing through the sample to obtain 2D transmission images of the pores and defect areas of the internal structure in a nondestructive manner. The electrode resistivities were measured using 46 multipoint probes connected to an electrode resistance measurement system (RM2610, HIOKI).

Cell Assembly: The as-prepared electrode was punched to a diameter of 12 mm with an average loading level of 7.1 mg cm $^{-2}$. To fabricate 2032-type half cell, a 12 mm-diameter Si/Gr electrode, a 14 mm-sized Li metal foil, and 18 mm-diameter polyethylene separator (PE, W-scope, 16 μ m thickness) with 1.0 M of LiPF $_6$ salt in ethylene carbonate/diethyl carbonate (3:7 in volume ratio) containing 10 wt% additional fluoroethylene carbonate were used. For the full-cell (Si/Gr||NCM622) assembly, a 12 mm-sized NCM622 cathode, 14 mm-sized Si/Gr anode, and 18 mm PE separator were combined with the same electrolyte used in the half-cell test.

Electrochemical Measurements: EIS (BioLogic VMP3) was used to verify the internal resistance of the assembled coin cells in the frequency range of 100–0. The half-cell cycling test of Li||Si/Gr was conducted in a voltage range of 0.005–1.5 V at 30 °C under 0.2 C rate. The cycling test of the Si/Gr||NCM622 full cell was evaluated in the voltage range of 2.8–4.3 V at 30 °C under normal conditions with 0.2 C rate followed by 0.1 C rate formation cycles. The rate capability test for both the half cell and full cell was conducted at C rate of 0.2 and 4.0 C rate.

Supporting Information

Supporting Information is available from the Wiley Online Library or from the author.

Acknowledgements

This work was supported by the Technology Innovation Program (RS-2024-00404166) funded by the Ministry of Trade, Industry and Energy (MOTIE/KEIT). This work supported by the research program of LOTTE Energy Materials.

Conflict of Interest

The authors declare no conflict of interest.

www.advancedsciencenews.com



www.small-structures.com

Author Contributions

Jeong Hyeon Yoo: Conceptualization (lead); Data curation (lead); Visualization (lead); Writing—original draft (lead). Sung Joon Park: Methodology (lead); Visualization (lead); Writing—original draft (lead); Writing—review and editing (lead). Cheol Bak: Data curation (lead); Software (lead). Yong Min Lee: Supervision (lead); Writing—original draft (lead); Writing—review and editing (lead). Ki Jae Kim: Conceptualization (lead); Data curation (lead); Supervision (lead); Writing—original draft (lead); Writing—review and editing (lead). Jeong Hyeon Yoo and Sung Joon Park contributed equally to this work.

Data Availability Statement

The data that support the findings of this study are available from the corresponding author upon reasonable request.

Keywords

bilayer electrodes, component gradients, electrode structures, porosity gradients, silicon/graphite anode

Received: August 14, 2024 Revised: November 1, 2024 Published online: November 21, 2024

- [1] G. Zubi, R. Dufo-López, M. Carvalho, G. Pasaoglu, Renewable Sustainable Energy Rev. 2018, 89, 292.
- [2] A. Väyrynen, J. Salminen, J. Chem. Thermodyn. 2012, 46, 80.
- [3] Y. B. Sim, H. Lee, J. Mun, K. J. Kim, J. Energy Chem. 2024, 96, 185.
- [4] S. J. Park, S. Y. Yang, S. A. Han, Y. J. Choi, T. Kim, M. S. Park, J. H. Kim, K. J. Kim, Chem. Eng. J. 2023, 460, 141620.
- [5] S. J. Park, Y. J. Choi, J. Cheon, H. Kim, J. W. Lee, T. Yim, K. J. Kim, J. Mater. Chem. A 2024, 12, 11551.
- [6] S. J. Park, Y. J. Choi, H. Seung Kim, M. J. Hong, H. Chang, J. Moon, Y. J. Kim, J. Mun, K. J. Kim, Carbon Energy 2024, 6, e487.
- [7] T. Yim, H.-J. Ha, M.-S. Park, K. J. Kim, J.-S. Yu, Y. J. Kim, RSC Adv. 2013, 3, 25657.
- [8] L. Wu, Y. Wang, X. Guo, P. Ding, Z. Lin, H. Yu, SusMat 2022, 2, 264.
- [9] X. Xu, X. Cheng, F. Jiang, S. Yang, D. Ren, P. Shi, H. Hsu, H. Yuan, J. Huang, M. Ouyang, Q. Zhang, SusMat 2022, 2, 435.
- [10] Y. Hou, R. Zhang, H. Cui, Q. Yang, C. Zhi, Exploration 2023, 3, 20220051.
- [11] Y. Li, Y. Qian, B. Deng, N. Lin, Chem. Eng. J. 2024, 488, 151012.
- [12] Y. Qian, Y. Liang, W. Zhang, B. Xi, N. Lin, Energy Storage Mater. 2023, 63, 102996.
- [13] Y. Li, Y. Qian, N. Lin, Y. Qian, Nano Res. 2022, 15, 230.
- [14] Y. Li, Y. Qian, Y. Zhao, N. Lin, Y. Qian, Sci. Bull. 2022, 67, 636.
- [15] J. Jang, H. Kim, H. Lim, K. J. Kim, H.-G. Jung, S.-O. Kim, W. Choi, Chem. Eng. J. 2020, 401, 126091.
- [16] L. Sun, Y. Liu, J. Wu, R. Shao, R. Jiang, Z. Tie, Z. Jin, Small 2022, 18, 2102894.
- [17] C. Zhang, F. Wang, J. Han, S. Bai, J. Tan, J. Liu, F. Li, Small Struct. 2021, 2, 2100009.
- [18] K. Xu, X. Liu, K. Guan, Y. Yu, W. Lei, S. Zhang, Q. Jia, H. Zhang, ChemSusChem 2021, 14, 5135.
- [19] M. Ashuri, Q. He, L. L. Shaw, Nanoscale 2016, 8, 74.
- [20] L. Sun, Y. Liu, R. Shao, J. Wu, R. Jiang, Z. Jin, Energy Storage Mater. 2022, 46, 482.
- [21] Q. Ma, Z. Zhao, Y. Zhao, H. Xie, P. Xing, D. Wang, H. Yin, Energy Storage Mater. 2021, 34, 768.

- [22] G. F. Pach, P. R. Adhikari, J. Quinn, C. Wang, A. Singh, A. Verma, A. Colclasure, J. H. Kim, G. Teeter, G. M. Veith, N. R. Neale, G. M. Carroll, ACS Energy Lett. 2024, 9, 2492.
- [23] X. Shen, Z. Tian, R. Fan, L. Shao, D. Zhang, G. Cao, L. Kou, Y. Bai, J. Energy Chem. 2018, 27, 1067.
- [24] X. Li, M. Zhang, S. Yuan, C. Lu, ChemElectroChem 2020, 7, 4289.
- [25] F. Dou, L. Shi, G. Chen, D. Zhang, Electrochem. Energ. Rev. 2019, 2, 149.
- [26] D. Liu, Y. Zhao, R. Tan, L. L. Tian, Y. Liu, H. Chen, F. Pan, Nano Energy 2017. 36, 206.
- [27] S. H. Lee, J. H. Lee, D. H. Nam, M. Cho, J. Kim, C. Chanthad, Y. Lee, ACS Appl. Mater. Interfaces 2018, 10, 16449.
- [28] H. Chen, Z. Wu, Z. Su, S. Chen, C. Yan, M. Al-Mamun, Y. Tang, S. Zhang, Nano Energy 2021, 81, 105654.
- [29] G. Huang, J. Han, Z. Lu, D. Wei, H. Kashani, K. Watanabe, M. Chen, ACS Nano 2020, 14, 4374.
- [30] C. Wang, F. Luo, H. Lu, X. Rong, B. Liu, G. Chu, Y. Sun, B. Quan, J. Zheng, J. Li, C. Gu, X. Qiu, H. Li, L. Chen, ACS Appl. Mater. Interfaces 2017, 9, 2806.
- [31] X. Li, M. Gu, S. Hu, R. Kennard, P. Yan, X. Chen, C. Wang, M. J. Sailor, J. G. Zhang, J. Liu, Nat. Commun. 2014, 5, 4105.
- [32] S. Chae, M. Ko, K. Kim, K. Ahn, J. Cho, Joule 2017, 1, 47.
- [33] P. Li, G. Zhao, X. Zheng, X. Xu, C. Yao, W. Sun, S. X. Dou, Energy Storage Mater. 2018, 15, 422.
- [34] S. He, S. Huang, S. Wang, I. Mizota, X. Liu, X. Hou, Energy Fuels 2021, 35, 944.
- [35] S. Chae, S. H. Choi, N. Kim, J. Sung, J. Cho, Angew. Chem. Int. Ed. 2020, 59, 110.
- [36] C. H. Yim, F. M. Courtel, Y. Abu-Lebdeh, J. Mater. Chem. A 2013, 1, 8234.
- [37] Z. Luo, Y. Xu, C. R. Gong, Y. Q. Zheng, Z. X. Zhou, L. M. Yu, J. Power Sources 2021, 485, 229348.
- [38] S. Liu, S. Cheng, M. Xie, Y. Zheng, G. Xu, S. Gao, J. Li, Z. Liu, X. Liu, J. Liu, B. Yan, W. Yan, Z. Zhang, G. Cui, J. Polym. Sci. 2022, 60, 1835.
- [39] O. Naboka, C. H. Yim, Y. Abu-Lebdeh, ACS Omega 2021, 6, 2644.
- [40] M. Choi, J. Sung, G. Yeo, S. Chae, M. Ko, J. Energy Storage 2023, 72, 108301
- [41] C. Jo, B. Wen, H. Jeong, S. K. Park, Y. Son, M. De Volder, ACS Nano 2023, 17, 8403.
- [42] Y. Cho, E. Lee, K. S. Lee, S. J. Hwang, C. W. Kim, T. G. Kim, S. K. Kang, S. Y. Park, K. Yoo, Y. Piao, Electrochim. Acta 2023, 447, 142134.
- [43] Z. Yan, S. Yi, X. Li, J. Jiang, D. Yang, N. Du, Mater. Today Energy 2023, 31, 101225.
- [44] E. Moyassari, L. Streck, N. Paul, M. Trunk, R. Neagu, C.-C. Chang, S.-C. Hou, B. Märkisch, R. Gilles, A. Jossen, J. Electrochem. Soc. 2021, 168, 020519.
- [45] M. P. Bonkile, Y. Jiang, N. Kirkaldy, V. Sulzer, R. Timms, H. Wang, G. Offer, B. Wu, J. Power Sources 2024, 606, 234256.
- [46] Z. Guo, L. Zhou, H. Yao, Mater. Des. 2019, 177, 107851.
- [47] W. Zhang, S. Gui, W. Li, S. Tu, G. Li, Y. Zhang, Y. Sun, J. Xie, H. Zhou, H. Yang, ACS Appl. Mater. Interfaces 2022, 14, 51954.
- [48] C. Bak, K. G. Kim, H. Lee, S. Byun, M. Lim, H. An, Y. Roh, J. Lim, C. B. Dzakpasu, D. Kim, J. Lee, H. Lee, H. Lee, Y. M. Lee, *Chem. Eng. J.* 2024, 483, 148913.
- [49] J. Shin, J. H. Lee, J. K. Seo, W. T. A. Ran, S. M. Hwang, Y. J. Kim, Int. J. Energy Res. 2022, 46, 16061.
- [50] J. Kim, M. H. Kim, Y. Kim, M. S. Kim, A. Choi, K. M. Jeong, H. W. Lee, Energy Storage Mater. 2023, 57, 269.
- [51] C. Heubner, T. Liebmann, O. Lohrberg, S. Cangaz, S. Maletti, A. Michaelis, Batter. Supercaps 2022, 5, e202100182.
- [52] A. Güneren, A. A. Nada, A. O. Šišková, K. Mosnáčková, A. Kleinová, J. Mosnáček, Z. Lenčéš, J. Appl. Electrochem. 2024, 54, 1409.
- [53] Y.-K. Ahn, Y. N. Jo, W. Cho, J.-S. Yu, K. J. Kim, Energies 2019, 12, 1638.